Data Mine

The Imperial Valley Dark Fiber Project: Toward Seismic Studies Using DAS and Telecom Infrastructure for Geothermal Applications

Jonathan Ajo-Franklin[*†1], Verónica Rodríguez Tribaldos[†2], Avinash Nayak[†2], Feng Cheng[†1], Robert Mellors[3], Benxin Chi[4], Todd Wood[2], Michelle Robertson[2], Cody Rotermund[5], Eric Matzel[6], Dennise C. Templeton[6], Christina Morency[6], Kesheng Wu[7], Bin Dong[7], and Patrick Dobson[2]

Abstract

The Imperial Valley is a seismically active basin occupying the southern end of the Salton trough, an area of rapid extension, high heat flow, and abundant geothermal resources. This report describes an ongoing large-scale distributed acoustic sensing (DAS) recording study acquiring high-density seismic data on an array between Calipatria and Imperial, California. This 27 km array, operating on dark fiber since 9 November 2020, has recorded a wealth of local seismic events as well as ambient noise. The goal of the broader Imperial Valley Dark Fiber project is to evaluate passive DAS as a tool for geothermal exploration and monitoring. This report is intended to provide installation information, noise characteristics, and metadata for future studies utilizing the data set. Because of the relatively small number of basin-scale DAS studies that have been conducted to date, we also provide a range of lessons learned during the deployment to assist future researchers exploring this acquisition strategy.

Cite this article as Ajo-Franklin, J., V. Rodríguez Tribaldos, A. Nayak, F. Cheng, R. Mellors, B. Chi, T. Wood, M. Robertson, C. Rotermund, E. Matzel, *et al.* (2022). The Imperial Valley Dark Fiber Project: Toward Seismic Studies Using DAS and Telecom Infrastructure for Geothermal Applications, *Seismol. Res. Lett.* **93**, 2906–2919, doi: 10.1785/0220220072.

Introduction

As the world pivots toward energy resources with close to zero carbon emissions, the value of geothermal energy production is becoming more obvious, particularly for baseload and dispatchable electricity production during periods with low availability of intermittent renewables. This demand has generated a renaissance in exploration for geothermal resources, particularly "hidden" systems with no surface expression, for example, lacking thermal features such as fumaroles, geysers, or hot springs. In the past, these systems have often been located accidentally while drilling for hydrocarbons, mineral deposits, or groundwater; in these situations, hot water was discovered instead of the target resource. Many hidden systems exist in underexplored basins where the lack of petroleum exploration targets has resulted in more limited availability of commercial reflection seismic data sets and other data that might aid in the discovery of geothermal resources.

Although a host of geophysical signatures can be used as part of the exploration for hidden geothermal resources (e.g., Garg *et al.*, 2010; Dobson, 2016), a hydrogeothermal system needs to have a combination of high temperatures and mobile fluids (i.e., sufficient porosity and permeability) at shallow to intermediate depths to be economical with present drilling technologies. From a seismic perspective, relevant signatures indicative of permeable features might include low velocity zones (LVZ) or altered Poisson's ratios associated with highly fractured rocks at depth, higher seismic attenuation or unusual attenuation ratios (Q_P/Q_S), and zones of higher local seismicity indicative of

1. Department of Earth, Environmental, and Planetary Science, Rice University, Houston, Texas, U.S.A.; 2. Energy Geosciences Division, Lawrence Berkeley National Laboratory, Berkeley, California, U.S.A., https://orcid.org/0000-0002-1325-0434 (VRT); https://orcid.org/0000-0001-7913-7189 (AN); https://orcid.org/0000-0002-4790-0888 (TW); https://orcid.org/0000-0001-5031-8592 (PD); 3. Institute of Geophysics and Planetary Physics, Scripps Institution of Oceanography, UC San Diego, La Jolla, California, U.S.A., https://orcid.org/0000-0002-2723-5163 (RM); 4. State Key Laboratory of Geodesy and Earth's Dynamics, Innovation Academy of Precision Measurement Technology and Science, Chinese Academy of Sciences, Wuhan, China; 5. ESnet/Lawrence Berkeley National Laboratory, Berkeley, California, U.S.A.; 6. Lawrence Livermore National Laboratory, Livermore, California, U.S.A., https://orcid.org/0000-0002-9154-5596 (CM); 7. Lawrence Berkeley National Laboratory, Berkeley, California, U.S.A., https://orcid.org/0000-0002-6907-3393 (KW)

*Corresponding author: ja62@rice.edu

†These authors contributed equally to this work.

kinematic preservation of permeability through shear (e.g., Faulds and Hinz, 2015). Likewise, zones of higher seismic velocity can be indicative of hydrothermal alteration and in some cases map to areas with significant heat flow (Ryan and Shalev, 2014; McGuire *et al.*, 2015). Beyond exploration, once these geothermal systems are found, they require detailed characterization and monitoring to allow for efficient well targeting and safe exploitation, two goals facilitated by dense high-quality seismic networks and their resulting data sets.

Significantly, effective exploration for geothermal resources is often tightly tied to understanding basin-scale tectonic deformation, fault architecture, and hydrogeology. Faults often serve as conduits for deep hydrothermal fluids to migrate to shallower reservoirs; zones of fault termination and the resulting stress concentrations are related targets due to favorable transport conditions (e.g., Curewitz and Karson, 1997). Faulds and Hinz (2015) identified zones with overlapping fault strands or normal fault terminations as particularly useful targets when found in areas of high strain rate and extension. Likewise, slip on these fault systems can potentially preserve permeability through damage processes. Larger scale distributed deformation, and even structures deep in the crust (e.g., Siler and Kennedy, 2016), can also generate the fracture porosity and flow pathways required for sustainable hydrothermal production.

The Imperial Valley and Brawley seismic zone (BSZ)

The present project targets hidden systems and relevant structures in southern California's Imperial Valley, the southern section of the Salton Trough. The Salton Trough is an active pull-apart basin with zones of extension in a sequence of stepovers between the strike-slip San Andreas and Imperial Valley fault systems (Brothers *et al.*, 2009; Kaspereit *et al.*, 2016). The Imperial Valley is a region of very high heat flow (~140 mW/m^2, Lachenbruch *et al.*, 1985) and hosts a number of significant developed geothermal resources including the giant Salton Sea field and the smaller East Mesa, Heber, and Brawley fields; these systems cumulatively have a current net installed capacity of ~605 MWe (Robertson-Tait *et al.*, 2021). At present, the U.S. Geological Survey (USGS) estimates that another 8.79 GWe of undiscovered systems still exist in the basin (Williams *et al.*, 2009), a strong motivation for the development of improved high-resolution exploration tools.

The Brawley geothermal system is one such hidden resource, discovered in 1963 while drilling an exploratory oil well (Brook and Mase, 1981). The first phase of development at Brawley occurred in the late 1970s when Unocal and Southern California Edison utilized a hot (274 °C) highly fractured reservoir at 1500–2150 m depth to produce about 10 MWe using a flash plant (Cedillo and Yamasaki, 1981; Matlick and Jayne, 2008). This plant was eventually closed due to extensive scaling and corrosion problems generated by the ~125,000 ppm total dissolved solids (TDS) high temperature brines. Ormat subsequently redeveloped a shallower (510–1370 m), lower salinity (21,000–45,000 ppm TDS), and cooler (~180 °C) resource dominated by matrix permeability; this resource is now producing brine utilized by a 50 MWe binary power plant (Matlick and Jayne, 2008).

The Brawley field is coincident with the Brawley fault zone, a region incorporating several seismically active en echelon fault strands at the southern end of the BSZ but north of the terminus of the Imperial Valley fault. The relationship between the BSZ and the deeper fractured geothermal system is still enigmatic despite considerable study. Links may exist between stress changes related to geothermal production and deeper aseismic slip (Wei *et al.*, 2015; Im and Avouac, 2021). Likewise, relocations of the primary event and aftershock sequence from the 2012 Brawley sequence appear to delineate an intermediate-depth fault beneath the field, coincident with mapped surface rupture traces trending southwest–northeast (Hauksson *et al.*, 2013). These observations provide a dual motivation to better understand the underlying structure of the Brawley field, to both elucidate the relationship between the fault system and the origin of the deep geothermal resource as well as to evaluate any production and injection-related induced-seismicity hazards.

Challenges of seismic exploration in geothermal provinces

A significant challenge for geothermal exploration is the lack of dense high-quality multiclient seismic data on the regional scale in the most relevant basins. In contrast with petroleum exploration provinces, reflection coverage of the relatively shallow high-heat flow basins is often sparse and limited to vintage 2D profiles. 3D survey coverage is unusual as are long-offset studies targeting scattering features deep within crystalline basement units.

A large portion of the deep seismic structural constraints available in the Imperial Valley comes from a nearly half century history of academic active source refraction and reflection surveys, starting with the work of Fuis *et al.* (1982, 1984) and continuing with the basin-wide Salton Sea Seismic Imaging Project (SSIP), conducted in 2011. The SSIP effort utilized a large hybrid 2D/3D array of over 4500 4.5 Hz geophones, a linear broadband profile (30+ sensors), and 126 explosive shot points to constrain structure in both the Imperial and Coachella valleys (Han *et al.*, 2016; Persaud *et al.*, 2016; Fuis *et al.*, 2017). These measurements, coupled with a relatively robust regional seismic network designed for earthquake seismology applications, provide an excellent starting point for investigating the smaller scale structures potentially associated with individual geothermal fields. Seismic surveys have been conducted on more local scales in the Imperial Valley area by geothermal exploration groups with the objective of identifying permeable fault targets; these efforts identified numerous faults in

the area but did not lead to the drilling of successful geothermal wells (e.g., Ram Power, Inc., 2013; Ormat Nevada Inc., 2017).

Distributed acoustic sensing (DAS) and dark fiber as a sensing resource

Over the last decade, DAS has been rapidly adopted as an approach for large-*N* seismic acquisition (Zhan, 2020; Lindsey and Martin, 2021). DAS utilizes short pulses of laser light to measure changes in Rayleigh backscattering within a continuous fiber-optic cable; these changes are then localized in space using a time-to-distance transform (Hartog, 2000) over an averaging domain referred to as the gauge length. DAS effectively transforms a strand of fiber into a dense array of extensional strain or strain-rate sensors spanning up to 10 s or low 100 s of kilometer with spatial resolutions down to the meter scale, depending on the optical parameters selected. Although originally used primarily for exploration and reservoir monitoring targets in the context of active-source vertical seismic profiling (e.g., Mateeva *et al.*, 2012; Daley *et al.*, 2013; Correa *et al.*, 2017), the approach was quickly adopted for classical seismology applications in a variety of array geometries (Lindsey *et al.*, 2017; Li and Zhan, 2018, Wang *et al.*, 2018; Nayak *et al.*, 2021). A strength of most DAS sensing systems is the broad bandwidth of the resulting measurements, spanning the exploration seismic range (1–100 Hz; Miller *et al.*, 2016), through the regional and teleseismic bands (1–100 s; e.g., Yu *et al.*, 2019; Lindsey, Rademacher, and Ajo-Franklin, 2020), all the way down to periods most relevant to geodetic and tidal measurement (1000 s; e.g., Becker *et al.*, 2017). This impressive measurement bandwidth, when coupled to high measurement density and spatial extent, positions DAS as a powerful tool for seismological sensing (Paitz *et al.*, 2021).

The majority of the examples discussed earlier utilize fibers deployed as fit-for-purpose sensing networks. Although fiber-optic cables are relatively inexpensive on an effective per-sensor basis, the installation of larger arrays (multikilometer) can be cost-prohibitive due to the challenges of permitting, trenching, and land access. Fortunately, a vast number of linear kilometer of fiber is already installed in the subsurface as part of the international telecommunication network. Components of the network that are not currently utilized for communication purposes are referred to as "dark fiber" and can be purchased, or more commonly, leased from existing telecommunications operators. Several studies have demonstrated the use of this existing network for geophysical measurements, including seismicity and ambient noise measurements (Jousset *et al.*, 2018; Ajo-Franklin *et al.*, 2019), aftershock studies (Li *et al.*, 2021), deep crustal imaging (Yu *et al.*, 2019), and even time-lapse measurements of aquifer processes (Rodríguez Tribaldos and Ajo-Franklin, 2021). The approach has been demonstrated in terrestrial environments, in both rural and urban contexts (Lindsey, Yuan, *et al.*, 2020; Zhu *et al.*, 2021), as well as with marine cables (e.g., Lindsey *et al.*, 2019).

From a methodological perspective, DAS deployed on telecom fiber can be utilized in several modes for geophysical imaging and monitoring, including approaches that are challenging for sparser regional networks. The dense large-*N* nature of DAS arrays is a perfect match for high-resolution ambient noise studies employing higher frequency bands (e.g., Williams *et al.*, 2021); likewise, the high spatial sampling allows for identification of reflected and scattered modes from passive sources including scattered surface waves (e.g., Cheng *et al.*, 2021) that might be spatially aliased when recorded by sparse networks.

The goals of the Imperial Valley Dark Fiber (IVDF) project are multiple and include (1) evaluation of the combination of DAS and dark fiber for geothermal exploration at the basin to field scale, (2) development of new DAS, array-based processing methods to exploit high density, passive seismic measurements for structural imaging, and (3) evaluation of the potential of DAS and dark fiber for detection of small-magnitude seismic events associated with geothermal production. The project will also evaluate the potential for detecting shallow thermal anomalies associated with underlying geothermal systems using distributed temperature sensing in dark fiber arrays—this capability would permit basin-scale evaluation of such features and would augment existing point measurement technologies (e.g., Zehner *et al.*, 2012).

Experiment Design and System Deployment

Design and deployment of the IVDF array required about a year from concept to first data retrieval. Significant steps included initial fiber resource discovery and contracting, system installation, and fiber mapping.

Fiber access and experiment geometry

An initial challenge for the project was locating a section of subsurface telecom fiber relevant to our imaging target. In the Imperial Valley, existing fiber is owned by a combination of major telecom providers, local operators, and not-for-profits serving community institutions. An additional issue, from a geophysical sensing perspective, is that several long-haul fiber paths are installed aerially (on telephone and/or power poles) rather than in the subsurface, eliminating their utility for seismology. In addition to fiber access, dark fiber recording efforts also requires environmentally controlled rack space for long-term interrogator unit (IU) deployments; many fiber-optic connection locations are of insufficient size to house complete systems, hence this issue should not be neglected during the DAS siting stage.

After discussions with several providers, we secured access to an L-shaped fiber section that traverses the BSZ starting in Calipatria, through Brawley and Imperial, California, and then turns west at El Centro, terminating in Plaster City. Figure 1 shows the fiber path with respect to mapped Quaternary faults, historical seismicity, and the regional seismic network.

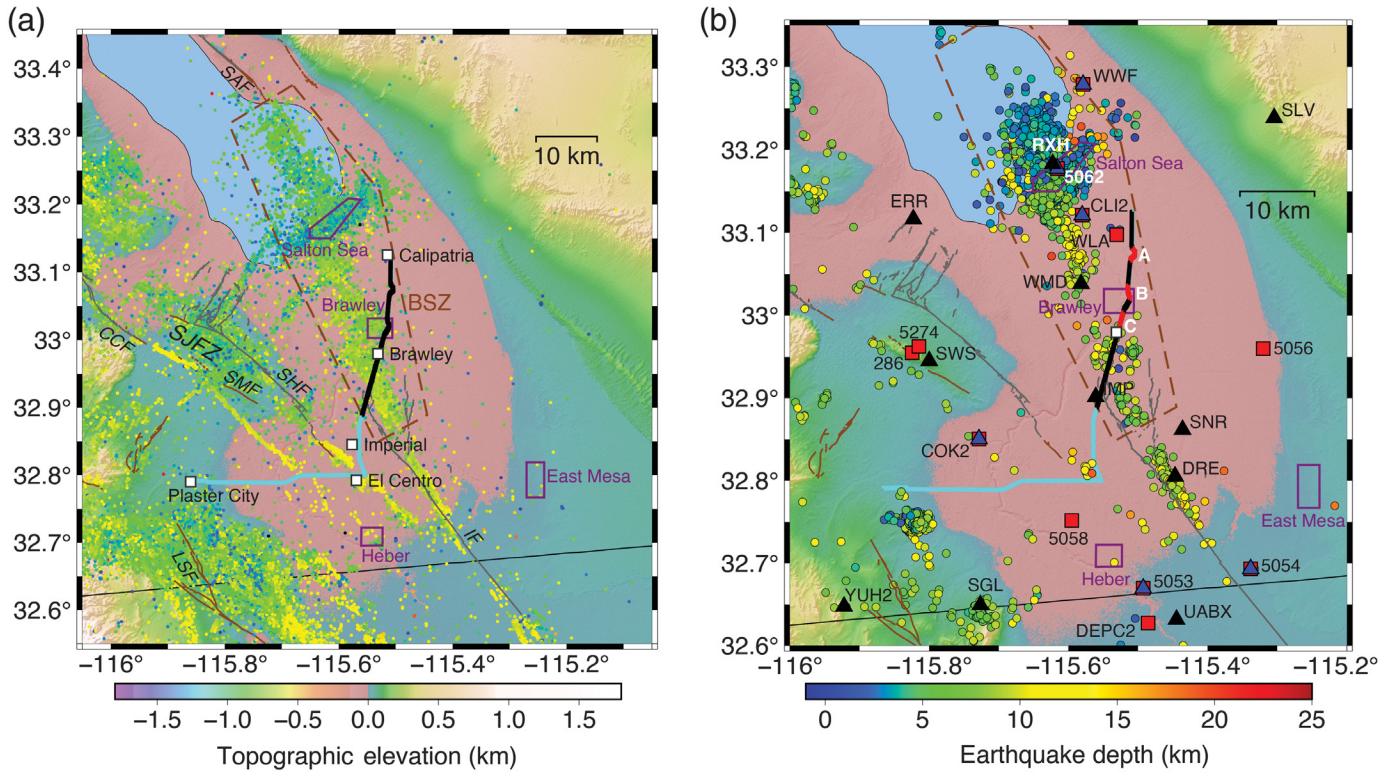

Figure 1. (a) Seismotectonic map of the study area. Circles color coded by depth show historical seismicity from the revised version (1981–2019) of the Hauksson *et al.* (2012) catalog. The cyan line is the fiber path. Distributed acoustic sensing (DAS) data were acquired along the northern section of the cable (black segment, ~28 km length) in this study. The purple polygons outline major producing geothermal fields. Other features are cities (white squares), Brawley seismic zone (dashed brown polygon), historical faults (brown lines), and Holocene to latest Pleistocene faults (gray lines) from the U.S. Geological Survey and California Geological Survey fault database. The major faults are Brawley seismic zone (BSZ), Coyote Creek fault (CCF), Imperial fault (IF), Laguna Salada fault (LSF), San Andreas fault (SAF), Superstition Hills fault (SHF), San Jacinto fault zone (SJFZ), and Superstition Mountain fault (SMF). (b) Slightly expanded view of the region shown in panel (a). Circles color coded by depth show seismicity during the period of DAS data acquisition (20 November 2020–July 2021) from the Southern California Earthquake Data Center (SCEDC) catalog. Permanent seismic stations (names indicated)—broadband sensors (black triangles), vertical component short-period sensor (blue triangles), accelerometer (red squares). The red segments on the DAS array (marked A, B, C in white) are used in noise analysis shown in Figure 5.

The total path length (~65 km, cyan curve in Fig. 1) is too long for DAS monitoring using the IU we selected for the experiment; only the first 28 km, shown in solid black, are effectively recorded, which will be discussed subsequently, with the final zone of recording slightly south of the Imperial Valley fault intersection. This path fulfilled our primary project requirements in that it (1) traversed a previously hidden geothermal resource (the Brawley field), (2) sampled an important portion of the BSZ fault architecture, and (3) covered a sufficient linear extent to experiment with new array processing approaches for regional seismic observations.

The array was also advantageously positioned with respect to the regional seismic network and included a permanent broadband station less than 500 m off the profile (CI.IMP, see Fig. 1) and several similarly spaced strong-motion stations (e.g., NP.5061, SB.WLA) to provide direct sensor comparisons to DAS. The fiber profile is also colinear with a moderately active railroad corridor that we hope will prove advantageous from an ambient noise imaging perspective. Trains can be exploited as powerful seismic sources for both static imaging (Quiros *et al.*, 2016; Ajo-Franklin *et al.*, 2019) as well as dynamic monitoring applications (Brenguier *et al.*, 2019; Pinzon-Rincon *et al.*, 2021).

System installation at Calipatria

The DAS IU and associated support instrumentation was installed on 9 November 2020 in an intermediate light amplification (ILA) hut in Calipatria, California (see Fig. 2a). ILA huts are telecom facilities providing access to long-haul fiber between major hubs and typically provide power and rack space that can house switches or, in the case of geophysical studies, DAS equipment. The DAS IU was installed on a vibration isolated table (Model B1824F, Thorlabs Inc.) within a small portable rack unit to mitigate acoustic noise from nearby colocated systems (see Fig. 2f). In addition to the DAS IU

Figure 2. Field installation and system montage. (a,b) the Calipatria, California, intermediate light amplification (ILA) hut and a tap test location, respectively; (c) installation of the Global Positioning System antenna and external environmental monitoring sensor; (d–f) the first recorded data, interrogator unit (IU) configuration process, and IU monitoring system stack, respectively. UPS, uninterruptible power supply.

(iDAS v2. Silixa LLC), we deployed a small local network switch, a server, a remotely controllable uninterruptible power supply, a RAID-6 array for storage (Model TS-1273U-8 G-US, QNAP Systems Inc.), and a pair of cellular-to-internet bridges to provide telemetry. The RAID system was a 12-bay (8 TB/bay), 2U rack mount unit designed with a 90 TB storage capacity, sufficient space for approximately 5 months of recording between data harvesting trips. Figure 2 shows several images from the installation process and the final system configuration as well as the acquisition electronics stack utilized in the experiment. Timing was provided by a Global Positioning System (GPS) antenna routed through an ILA external access duct. An environmental monitoring system (Hobo, Onset) was also installed to measure temperature in the DAS chassis, air circulating in the ILA, and outside of the building; we should note that low-frequency DAS strain measurements can be sensitive to interrogator temperature, and the environmental state of the IU should be monitored as a best practice, similar to long period seismic instrumentation.

Acquisition parameters and telemetry

After several acquisition tests, we decided to record at 500 Hz using a 4 m channel spacing and a total array channel account of 6912, equivalent to a 27.6 km linear array length. The relatively high sampling rate of 500 Hz was selected to allow for high-frequency ambient noise analysis and to quantify optical noise levels during recording. The DAS IU utilized has a gauge length of 10 m and records in strain rate; we should note that the laser pulse rate was 2 kHz, higher than the sampling rate, to improve system dynamic range. Continuous records were recorded in 1-min blocks in HDF-5 format; each record was approximately 415 MB in size. We have found this file size to be a reasonable compromise, large enough to allow useful single file quality control analysis and small enough to be transferred using lower bandwidth telemetry links.

When operating at these acquisition parameters, the IVDF array generates approximately 0.6 TB/day. This is a data volume that, although large, could be accommodated by a high-quality fiber link. Unfortunately, the absence of accessible switching infrastructure at the ILA prevented us from streaming the full data set. The only telemetry that could be established at the initiation of the experiment was a pair of cellular links to our DAS data local area network. These links exhibit variable performance, but average 1.5 MB/s, sufficient to download 1-min records over an ~10-min period; however, the systems were also throttled based on bandwidth usage and could effectively be utilized to download only 20–30 records per day. Based on this limitation, we largely used the telemetry link to evaluate instrument state-of-health, check RAID utilization, and download specific seismic events detected on the regional network.

Tap testing for establishing geometry

Unlike classical point sensors in which the measurement location and vector component orientation is easily established using GPS or other surveying approaches, establishing the network geometry for telecom-based DAS acquisition is a more involved process. A first aspect worth noting is that

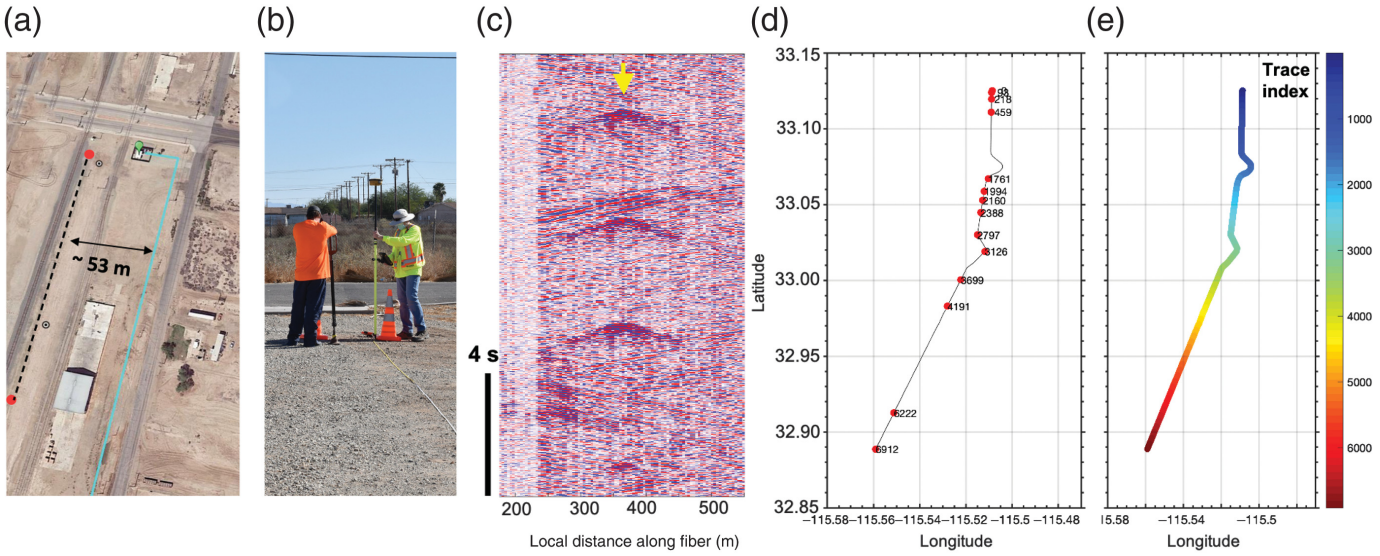

Figure 3. Tap test for establishing geometry: (a) common case where vendor provided fiber location (cyan line) is offset from the actual fiber path (dashed black line); (b,c) tap test execution and typical DAS response; (d,e) the channel number to latitude/longitude mapping result.

the DAS measurement optically probes the fiber in a purely linear sense; if a coil of slack fiber exists along the profile, the channels in the slack coil are included in the sensing array. A second aspect is that the physical fiber profile is often known only approximately at the initiation of the survey, whereas we had a Geographic Information Systems layer with approximate locations, and it proved to be incorrect by as much as 50 m (Fig. 3a).

To establish a more accurate geometry, we conducted tap tests. Using our initial map as a starting point, 26 locations along the profile were scouted and surface markers were used to determine the actual fiber burial location in 2D. Figure 3b shows a map of the initial tap locations. Then, a small impact source (hammer) was used to facilitate identification of the corresponding channel number on the DAS array. Figure 2b shows one such tap testing location. These measurements were then interpolated to provide a mapping from array optical distance to physical location (Fig. 3c–e). The accuracy of this estimate is related to the number of channels the impact source is visible over as well as the linear distance to the nearest control point; we estimate our absolute accuracy is on the order of 1–2 gauge lengths (10–20 m) with some degree of variability across the array. The relative distance between channels is, of course, a much more accurate quantity except when jumps exist due to fiber slack at select locations.

Data Extraction for First Period and Quality Control

Initial data retrieval and processing environments

In the spring of 2021, after the first four months of recording, the portable disk array was swapped to allow access to the full continuous data set. Except for several short periods of downtime due to software problems, data were recovered for the entire period between 10 November 2020 and 23 March 2021. As mentioned previously, the data consisted of consecutive 1-min HDF-5 files; after retrieval, the data were uploaded to an enterprise RAID server at Lawrence Berkeley National Laboratory (LBNL) and then mirrored to a similar RAID server at Rice University to provide a geographically distributed backup. Both RAID servers were connected via local 10 GB links to high performance computing (HPC) clusters used for data processing, the Lawrencium HPC facility at LBNL (~23,000 cores) and the NOTS HPC facility at Rice (~6500 cores).

Example of array noise levels

Initial evaluation of noise levels on the array were promising. Immediately after deployment, the first day of data was utilized to map random and coherent noise sources across the 27 km of acquisition aperture. Figure 4c shows a typical time-domain record from the DAS array covering 60 s of continuous data. As can be seen from Figure 4c, a combination of vehicle noise and persistent noise sources are visible across the array. Toward the north end of the line, several large-scale agricultural facilities (Fig. 4a) generate persistent noise whereas a highway overpass and warehouse complex near Brawley (Fig. 4b) produces strong coherent Rayleigh waves, visible multiple kilometers away. Toward the southern end of the array, optical noise begins to dominate the recording, but intermediate magnitude seismic events are still visible.

Analysis of noise spectral components

Noise characteristics vary significantly across the array, ranging from strong anthropogenic signals near the towns of

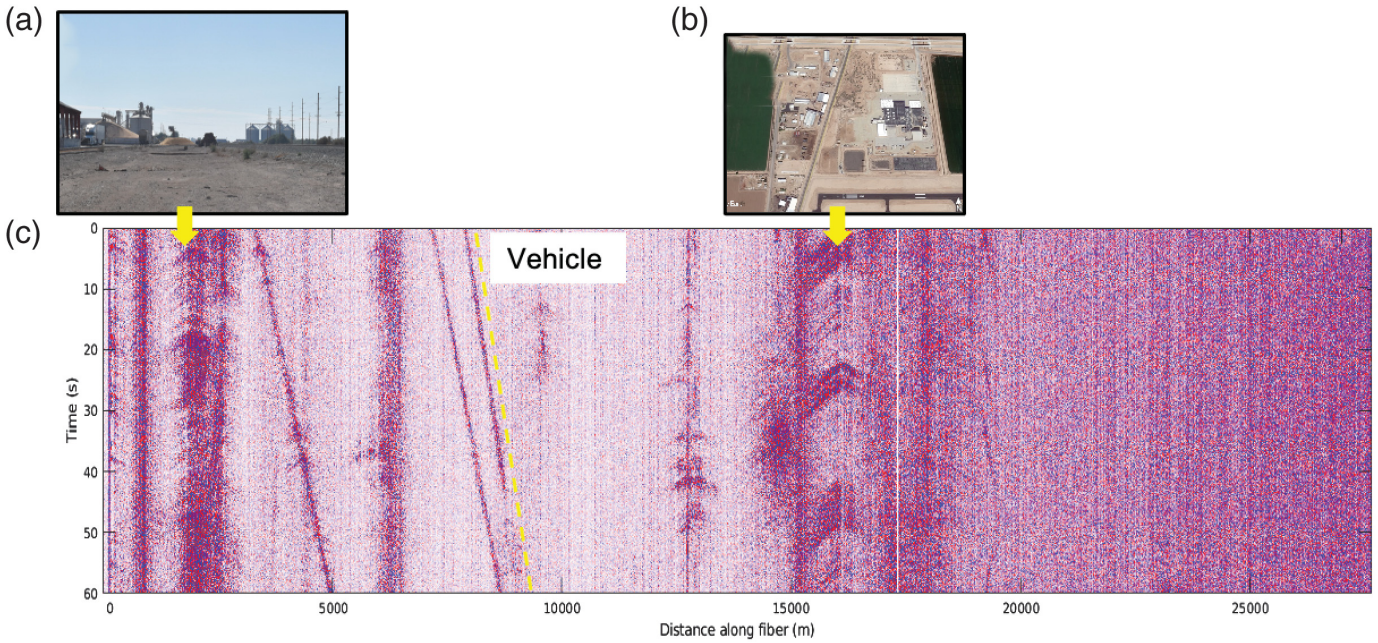

Figure 4. Noise scape over profile and persistent sources: (a,b) two sources of persistent noise (grain handling facility and highway overpass) superimposed on a (c) 60 s time domain gather.

Calipatria and Brawley to slightly quieter regions in the array interior. Figure 5 shows a week of power spectral density (PSD) measurements for three locations across the array including a section near Calipatria (Fig. 5a, channel [ch.] 1300–1800), a section near the Brawley geothermal field (Fig. 5b, ch. 2600–3100), and a section near the town of Brawley (Fig. 5c, ch. 3600–4100). In each plot, PSDs for each channel are computed for an hour and stacked to yield sequential hour records for a week of calendar time.

In all locations, the dominant noise peaks are in the 1–20 Hz band containing traffic and industrial noise sources. The anthropogenic noise signals are strongly diurnal, starting in the morning hours (5–6 a.m., local time) and decreasing in the evening (7 p.m.), with a minimum in the early morning (2–3 a.m.). A weekly cycle is also visible with lower noise levels on the weekend, particularly Sunday, which might be expected. A continuous secondary microseism peak is visible at all times at close to a 10 s period.

Initial Seismic Event Observations

A variety of earthquakes including local, regional, and teleseismic events were clearly recorded by the DAS array. Although data for a number of events were downloaded immediately after being cataloged by the Southern California Earthquake Data Center (SCEDC) and National Earthquake Information Center, a more detailed study was not possible until the RAID retrieval described previously.

The study area and the surrounding regions experience intense seismicity as a result of right-lateral strike-slip motion accompanied by transtensional tectonics (e.g., Elders *et al.*, 1972; McGuire *et al.*, 2015). Significant seismicity is broadly distributed over the BSZ. Most of the local seismicity during our deployment was generated by event clusters near Westmorland, Brawley, Ocotillo, the Salton Sea geothermal field, and along the Imperial Valley fault, as can be seen in Figure 1b. We also recorded a significant seismic swarm in June 2021 near the Salton Sea geothermal field that included 1800 recorded earthquakes (with 46 **M** ≥3 earthquakes) within a 9-day period.

We assembled a DAS waveform data set for all earthquakes cataloged by the SCEDC over a local domain (latitude 32.2 : 33.6, longitude −116.2 : −114.9) during our deployment period. We extracted 2-min DAS records for all earthquakes spanning from 30 s before the catalog origin time to 90 s afterward. The bulk of these events were visible on the DAS array without significant processing beyond channel stacking, typically median stacks of five channels, and band-pass filtering. Figure 6 shows local events from several of these zones of elevated seismicity. As would be expected considering DAS sensitivity to strain rate along the axial direction of the fiber, *S* arrivals exhibit considerably higher signal-to-noise ratios on horizontal DAS arrays when compared with near vertically incident *P* waves, which have very small amplitudes in the horizontal plane. For small earthquakes, *P* waves are obvious only for earthquakes located close to the DAS array.

Phase observations

As can be seen in Figure 6a, a variety of coherent phases are visible across the array beyond *P* and *S* body-wave arrivals. Easily visible in the Niland event are a sequence of free surface reflections, likely the *PP*, *SS*, and even *SSS* phases. Although

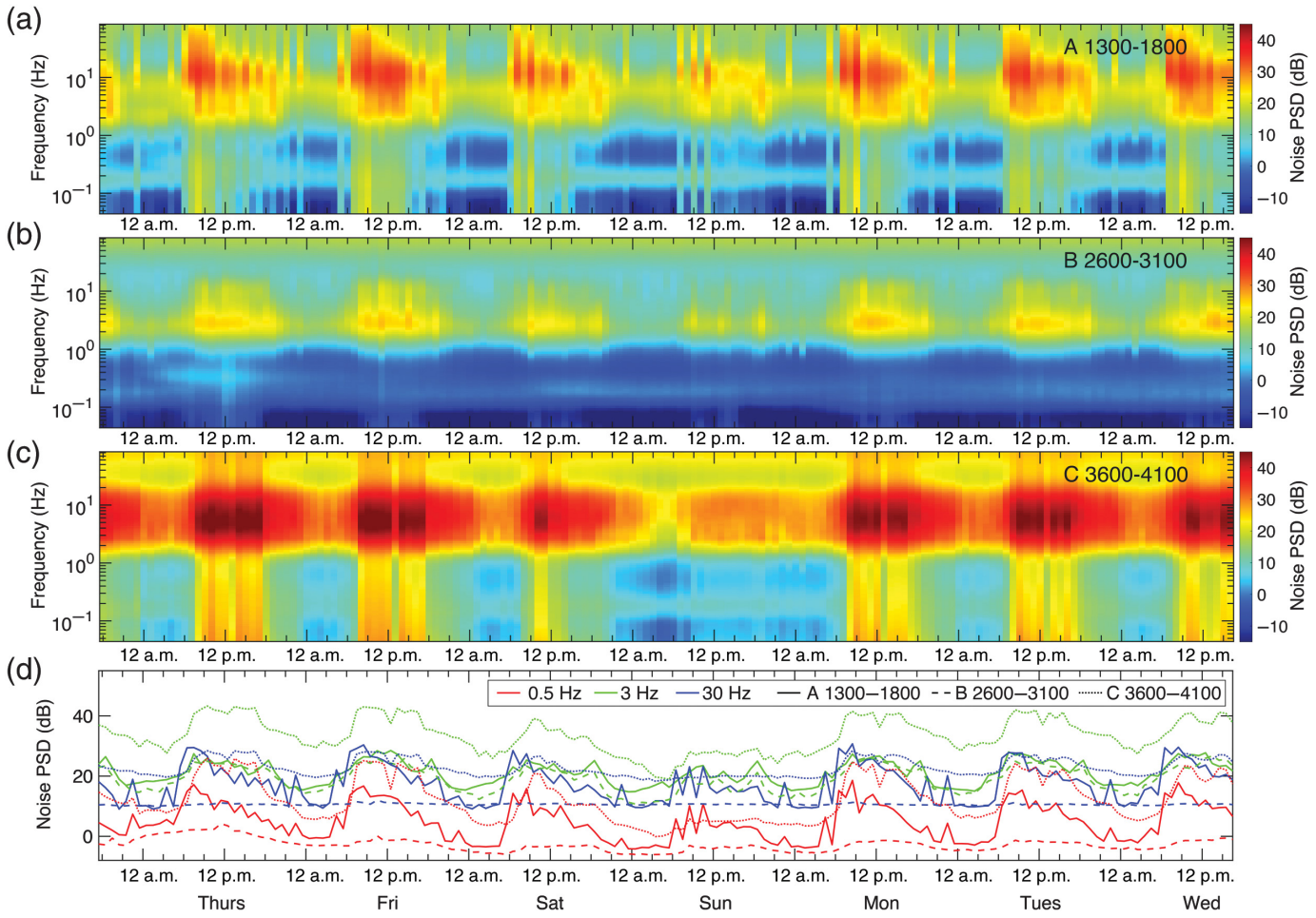

Figure 5. (a–c) Stacked hourly power spectral densities (PSDs) for three sections of the array over one week (03–10 December 2020, local time) as a function of frequency. (a) Channels 1300–1800 near Calipatria, (b) channels 2600–3100 near the Brawley geothermal field, and (c) channels 3600–4100 near the town of Brawley. The segments are marked in red on the DAS array in Figure 1b; (d) detailed variation of noise PSD with time at three discrete frequencies (color coded, see legend) for the three segments (solid: channels 1300–1800, dashed: channels 2600–3100, and dotted: channels 3600–4100).

such phases have been observed in the Imperial Valley as part of past studies due to the steep near-surface velocity gradient (e.g., Wei *et al.*, 2015), they are much simpler to identify with the dense spatial sampling available from the IVDF array. Likewise, utilization of the *SS* and *SSS* phases offers significant opportunities to improve ray-path coverage, particularly for shallow imaging targets.

Another interesting set of phases not mentioned in the literature are coherently scattered features originating near the Brawley field and the southern tip of the BSZ. These phases ("scattered phase ?" at along-fiber distance ~16–22 km in Fig. 6a,b) appear in events coming from a variety of azimuths; given the observed moveouts, they suggest a large lateral velocity contrast near the BSZ terminus, a prime imaging target to assist in resolving finer structures in the complicated zone near the field. In all of these cases, high energy phases observed on network station CI.IMP, close to the IVDF profile, were quite comparable (Fig. 6b, black waveform).

Regional and teleseismic events

Although the focus of this project is on basin-to-regional scale exploration, characterization, and monitoring, the bandwidth of DAS allows observations of regional and teleseismic events as well. Figure 7 shows a small subset of regional (Fig. 7a) and teleseismic (Fig. 7b) events sorted by epicentral distance. The events shown are single traces consisting of 100 channel stacks of the array (400 m segment between channels 2600 and 2700) including appropriate band-pass filters. Although the focus of our study is not these more distant events, their detectability across a range of distances and magnitudes is noted.

Clipping and Dynamic Range Observations during the June 2021 Salton Sea Swarm

As mentioned previously, the IVDF DAS deployment overlapped with an energetic seismic swarm that occurred during June 2021 near the Salton Sea. This swarm provided both a

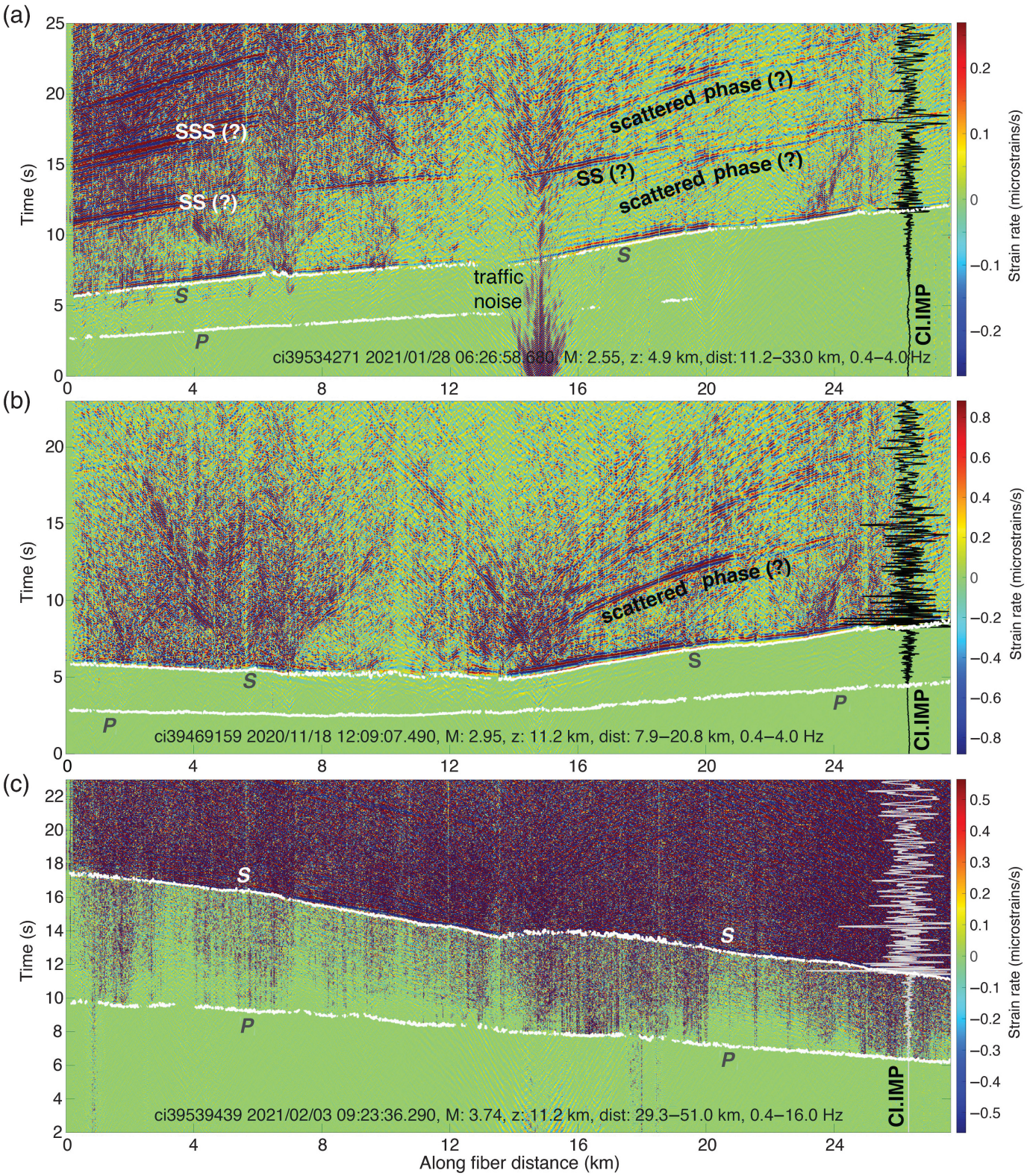

Figure 6. Record sections on the DAS array for three local earthquakes—(a) near Niland, (b) near Westmorland, and (c) near Ocotillo. *P*, *S* (white lines), and other possible coherent phases are marked. The event ID, origin time, magnitude, depth (*z*), epicentral distance range from the DAS array (distance) and the corners of the band-pass filtered are mentioned at the bottom of each plot. The seismograms overlain on the DAS record section at channel 6581 were recorded by the broadband sensor at seismic station CI.IMP, ~0.5 km from the DAS array. DAS waveforms in panel (c) have been filtered at higher frequencies compared with those described in panels (a) and (b), showing the *P* waves clearly.

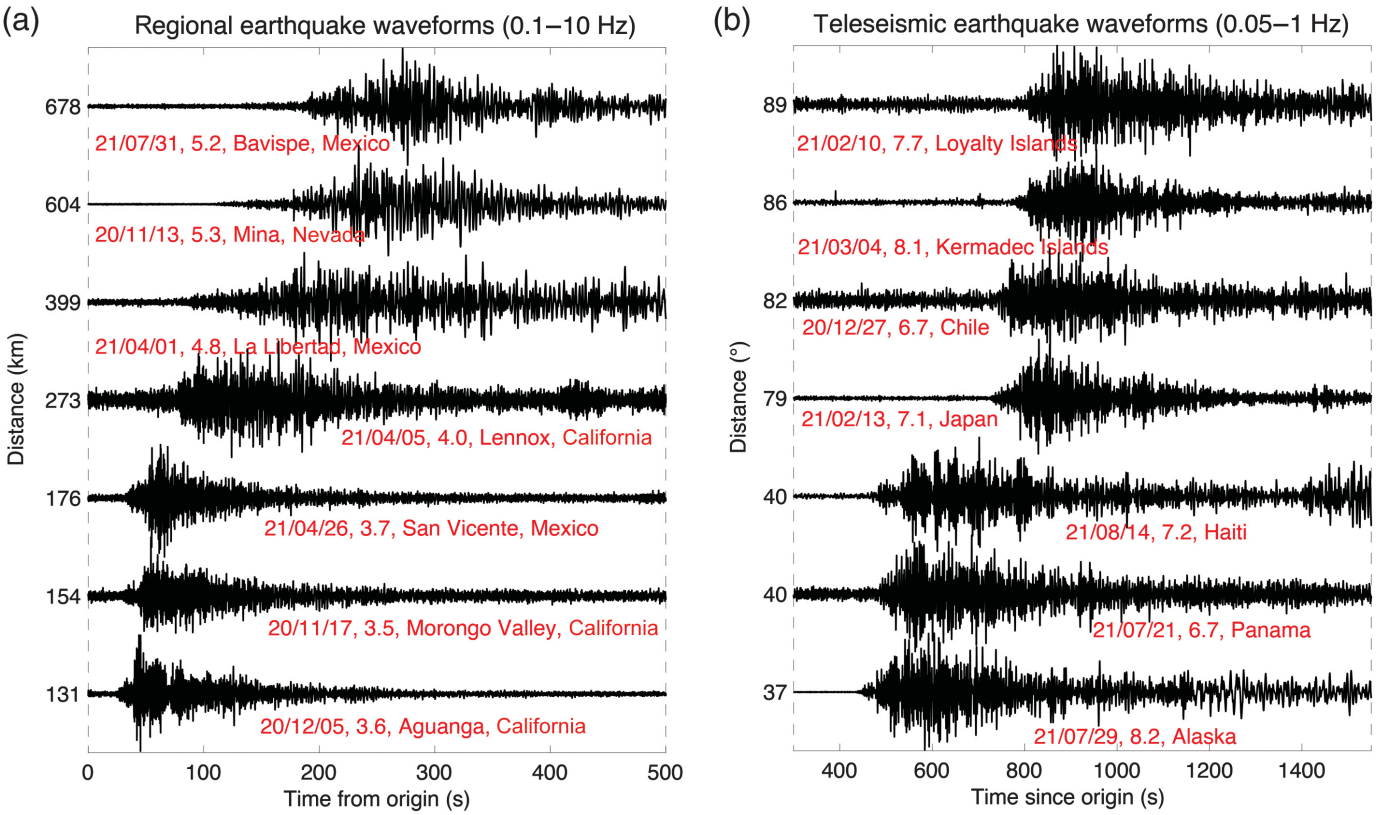

Figure 7. Example waveforms of (a) regional and (b) teleseismic earthquakes recorded by the DAS array. The waveforms are stacks of channels 2600–2700. For each earthquake, the origin date, magnitude, and geographical region are mentioned below the waveforms. Note the different time scale and band-pass filter used (mentioned on top) for the two sets of waveforms.

large number of local events to support our passive imaging efforts as well as an opportunity to explore magnitude estimation and the dynamic range limitations of DAS recording. Although dynamic range limitations for traditional inertial sensors (e.g., geophones) and analog-to-digital converters are widely studied and understood by the geophysical community, the same limits for DAS and other optical seismology approaches are less discussed. Unlike analog inertial sensor measurements, DAS and related technologies measure optical phase, which is then converted to strain or strain rate depending on the design of the IU.

The DAS IU we utilized returns the wrapped phase in the range $(-\pi, \pi)$, and when the strain rate exceeds 2π between sample points, the signal is saturated. The exact dynamic range is a function of both the internal laser repetition rate (which is higher than the sample rate of the seismic record in most cases) and the gauge length. The maximum laser repetition rate is in turn constrained by the total fiber length because the detector must wait for returning scattered energy before launching a new pulse at the same wavelength. In our case, the relatively long fiber length (~28 km) forced a somewhat lower pulse repetition rate and resulted in lower dynamic range.

This behavior differs from the "clipping" observed on standard seismic sensors due to dynamic range limitations of the sensor or digitizer. Specifically, when a DAS signal exceeds the dynamic range, the signal should flip from maximum to minimum. It may be possible, with additional postprocessing, to unwrap the 1D signals. Phase is not tracked in an absolute sense between consecutive laser pulses, and it is not possible currently to apply 2D phase unwrapping, as is done with interferometric synthetic aperture radar. One key to identifying saturated channels is low correlation between adjacent channels, even when the channel spacing is less than a gauge length.

The Salton Sea swarm of 2021 started on 5 June and included events as large as an **M** 5.25, seven events of **M** 4 +, 42 events of **M** 3 +, and a total of 1962 events in the USGS catalog. Events were clustered along two linear features, one trending northeast to southwest, south of the Salton Sea shore and a second trending north into the southern section of the sea. Many swarm events were only 8–12 km from the northern end of the IVDF DAS array and were thus easily detected, even lower magnitude events not present in the catalog.

Figure 8 shows a range of events from the swarm as recorded by different zones of the array for different magnitude events at similar locations. As can be seen, the entire array clips for the **M** 5.3 mainshock with traces flipping between the maximum and minimum phase until deep in the coda. **M** ~3–4 events exhibit different levels of clipping depending on hypocentral distance. Records of **M** <3 earthquakes are generally

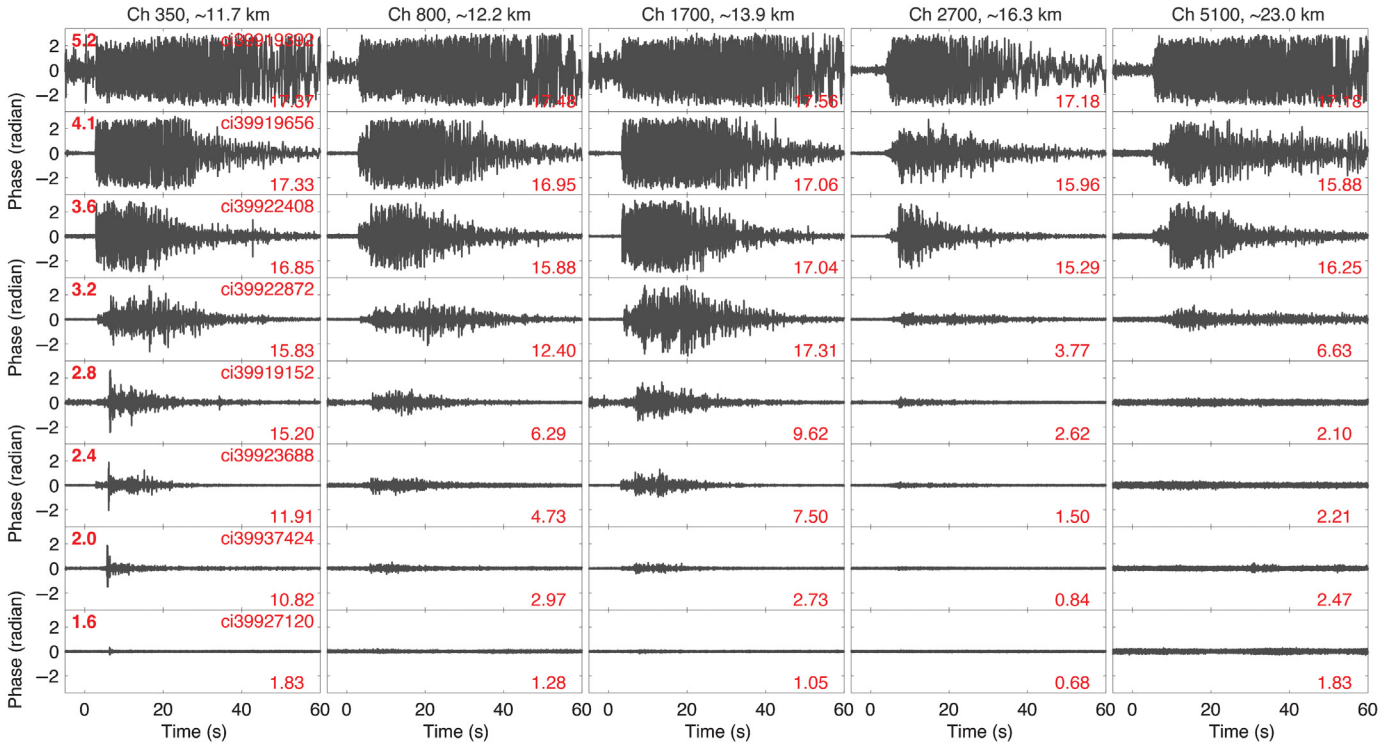

Figure 8. DAS data for different earthquakes (row-wise plots) in the June 2021 swarm recorded at different channels (column-wise plots). Epicentral distance increases from the northern section of the DAS array (left most column) to the southern section (right most column). Channel number and the median epicentral distance for the eight earthquakes (eight rows) are mentioned at the top of each column. Magnitude of the earthquakes decreases from the top row to the bottom row (magnitude is mentioned at the top left corner of the plot in the first column of each row). We show raw waveforms in units of radians; therefore, all amplitudes are restricted to $(-\pi, \pi)$. Peak values are indicated on bottom right corner of each plot.

unclipped at these distances. The smallest earthquake (**M** 1.6) in Figure 8 is obvious in the raw data only at the closest channel. The noise level generally increases toward the end of the DAS array (rightmost column) due to insufficient number of backscattered photons.

In the case of the Imperial Valley array and our particular acquisition parameters, clipping makes amplitude-based magnitude estimation difficult for large local events but coda duration magnitude estimation may still be possible (e.g., Gök *et al.*, 2016). This observation could be significant for future studies that hope to utilize DAS recordings for strong motion studies or aftershock monitoring following very large earthquakes.

Summary and Lessons Learned

As we have documented in this study, the combination of DAS and unused telecom fiber can provide a powerful sensing tool for high-resolution seismic acquisition at the basin scale. Although several past projects have demonstrated aspects of this technology combination (e.g., Jousset *et al.*, 2018; Ajo-Franklin *et al.*, 2019; Li *et al.*, 2021), few have deployed it at the basin scale targeting active fault systems, particularly over longer time durations (>1 yr). Although the geophysical results from the IVDF project are still a work in progress, a variety of lessons were learned during the deployment, some of which might prove useful in future campaigns of a similar nature.

Securing fiber access and DAS IU space

One barrier in the early phases of the project was obtaining fiber access. Although we were ultimately able to secure a good route, the time between selection of the target basin and DAS deployment was quite long (nearly a year). The challenge was finding a network operator with relevant fiber, subsurface coupling, and sufficient transmission quality (i.e., low loss) for DAS acquisition. Negotiation of contracts can also be time consuming, particularly with limited research budgets. Finally, not all fiber access locations (ILAs) have sufficient rack space to accommodate DAS IUs; once a path is found, access to the fiber from an appropriate space should also be determined.

Importance of timing and environmental monitoring

Past DAS projects utilizing dark fiber have suffered from the absence of GPS timing due to the positioning of the DAS in the interior of large network facilities without easy sky access (e.g., Ajo-Franklin *et al.*, 2019). This lack of accurate timing information hinders the identification of cataloged seismic events and complicates the comparison and integration of DAS

records with nearby seismic stations. Thus, an important consideration when choosing a deployment location for a DAS system is the feasibility of installing a GPS antenna that sees enough sky to provide accurate timing for the duration of the experiment. Besides timing, it is desirable to deploy the DAS system at a location where environmental parameters such as temperature and humidity can be controlled and monitored. Previous DAS projects have demonstrated that DAS IUs can be very sensitive to temperature variations. When analyzing low frequency (mHz or less) DAS records, temperature fluctuations at the location where the IU is deployed can introduce thermal strain signals that are observed along the entire fiber and mask the mechanical strain signals of interest.

Mapping fiber location

As mentioned previously, the initial vendor-provided map of fiber location was ultimately up to 50 m off the true physical location, thus necessitating a careful mapping phase. Although newer approaches using GPS-tracked vehicles may accelerate the process of constructing channel-to-fiber-location maps (e.g., Yuan *et al.*, 2021), this step should be incorporated as a key field activity in the early stages of acquisition.

Telemetry and data management

DAS systems running continuously generate substantial data volumes, particularly when recording at fine channel spacings and/or high temporal sampling rates. Because of the multifaceted targets in our project, we decided early on to record at reasonably high resolution to allow for near-surface imaging as well as microseismic event detection and location. As mentioned, we are currently exchanging intermediate scale RAID systems and using low-bandwidth cellular connectivity for quality control; future deployments could also consider edge compression and/or preprocessing as an attractive alternative.

Conclusions and Next Steps

Based on preliminary analysis of the IVDF data set, we expect the processed results to provide a variety of benefits for geothermal exploration and monitoring in the area. The quality of the ambient noise data set recorded is more than sufficient for high-resolution surface-wave imaging across the profile; we anticipate that this data product will provide useful constraints on zones of high and low V_S relevant to either areas of increased fracturing or zones of hydrothermal mineralization, respectively. Likewise, the existing and growing catalog of local seismic events will be useful for improved mapping of active and potentially transmissive faults as well as for body wave imaging to provide improved structural constraints. Finally, the abundance of spatially resolved scattered phases from local earthquakes offers new opportunities for high-resolution imaging.

Our next step in the project is execution of a large-scale nodal and sparse broadband deployment to explore hybrid seismographic networks and to better understand DAS array response. Upon conclusion of the experiment and publication embargoes, DAS data from the project will be made available on the Geothermal Data Repository.

Data and Resources

The majority of data shown was processed using in-house scripts developed in MATLAB (v.2020b, Mathworks). All distributed acoustic sensing data shown and the majority acquired in the project will be made available on the Geothermal Data Repository (https://gdr.openei.org/, last accessed June 2022) after publication embargoes are completed (Summer 2023). Waveform data for the Caltech Seismic Network (CI, doi: 10.7914/SN/CI) station IMP and the local earthquake catalog were downloaded from the Southern California Earthquake Data Center (doi: 10.7909/C3WD3xH1; http://scedc.caltech.edu/, last accessed September 2021). Some of the maps were prepared using Generic Mapping Tools (Wessel *et al.*, 2013).

Declaration of Competing Interests

The authors acknowledge that there are no conflicts of interest recorded.

Acknowledgments

The Imperial Valley Dark Fiber project was supported by the Office of Energy Efficiency and Renewable Energy, Geothermal Technologies Office, United States Department of Energy under Award Number DE-AC02-05CH11231 with Lawrence Berkeley National Laboratory (LBNL) and by Lawrence Livermore National Laboratory under Contract Number DE-AC52-07NA27344. The authors thank Thomas Coleman and Silixa LLC for useful acquisition suggestions and Zayo for fiber access and field support at the Calipatria intermediate light amplification. Karina Mellors and Dave Sandwell (UC San Diego) assisted with tap tests. This report was prepared as an account of work sponsored by an agency of the United States Government. Neither the United States Government nor any agency thereof, nor any of their employees, makes any warranty, express or implied, or assumes any legal liability or responsibility for the accuracy, completeness, or usefulness of any information, apparatus, product, or process disclosed, or represents that its use would not infringe privately owned rights. Reference therein to any specific commercial product, process, or service by trade name, trademark, manufacturer, or otherwise does not necessarily constitute or imply its endorsement, recommendation, or favoring by the United States Government or any agency thereof. The views and opinions of authors expressed therein do not necessarily state or reflect those of the United States Government or any agency thereof.

References

Ajo-Franklin, J. B., S. Dou, N. J. Lindsey, I. Monga, C. Tracy, M. Robertson, V. R. Tribaldos, C. Ulrich, B. Freifeld, T. Daley, *et al.* (2019). Distributed acoustic sensing using dark fiber for near-surface characterization and broadband seismic event detection, *Sci. Rept.* **9,** no. 1, 1–14.

Becker, M. W., C. Ciervo, M. Cole, T. Coleman, and M. Mondanos (2017). Fracture hydromechanical response measured by fiber optic distributed acoustic sensing at milliHertz frequencies, *Geophys. Res. Lett.* **44,** no. 14, 7295–7302.

Brenguier, F., P. Boué, Y. Ben-Zion, F. Vernon, C. W. Johnson, A. Mordret, O. Coutant, P. E. Share, E. Beaucé, D. Hollis, *et al.* (2019). Train traffic as a powerful noise source for monitoring active faults with seismic interferometry, *Geophys. Res. Lett.* **46,** no. 16, 9529–9536.

Brook, C. A., and C. W. Mase (1981). The hydrothermal system at the east Brawley KGRA, Imperial Valley, California, *Geotherm. Res. Council Trans.* **5,** 157–160.

Brothers, D. S., N. W. Driscoll, G. M. Kent, A. J. Harding, J. M. Babcock, and R. L. Baskin (2009). Tectonic evolution of the Salton sea inferred from seismic reflection data, *Nature Geosci.* **2,** 581–584.

Cedillo, R., and R. N. Yamasaki (1981). The Brawley 10 MWe power plant, unit 1, *Geotherm. Res. Council Trans.* **5,** 397–399.

Cheng, F., B. Chi, N. J. Lindsey, T. C. Dawe, and J. B. Ajo-Franklin (2021). Utilizing distributed acoustic sensing and ocean bottom fiber optic cables for submarine structural characterization, *Sci. Rept.* **11,** no. 1, 1–14.

Correa, J., A. Egorov, K. Tertyshnikov, A. Bona, R. Pevzner, T. Dean, B. Freifeld, and S. Marshall (2017). Analysis of signal to noise and directivity characteristics of DAS VSP at near and far offsets—A CO2CRC Otway project data example, *The Leading Edge* **36,** no. 12, 994a1–994a7.

Curewitz, D., and J. A. Karson (1997). Structural settings of hydrothermal outflow: Fracture permeability maintained by fault propagation and interaction, *J. Volcanol. Geotherm. Res.* **79,** nos. 3/4, 149–168.

Daley, T. M., B. M. Freifeld, J. Ajo-Franklin, S. Dou, R. Pevzner, V. Shulakova, S. Kashikar, D. E. Miller, J. Goetz, J. Henninges, *et al.* (2013). Field testing of fiber-optic distributed acoustic sensing (DAS) for subsurface seismic monitoring, *The Leading Edge* **32,** no. 6, 699–706.

Dobson, P. F. (2016). A review of exploration methods for discovering hidden geothermal systems, *Geotherm. Res. Council Trans.* **40,** 695–706.

Elders, W. A., R. W. Rex, T. Meidav, P. T. Robinson, and S. Biehler (1972). Crustal spreading in southern California, *Science* **178,** no. 4056, 15–24.

Faulds, J. E., and N. H. Hinz (2015). Favorable tectonic and structural settings of geothermal systems in the Great Basin region, western USA: Proxies for discovering blind geothermal systems, *Proc. of the World Geothermal Congress*, Melbourne, Australia, 19–25 April 2015, 6 pp.

Fuis, G. S., K. Bauer, M. R. Goldman, T. Ryberg, V. E. Langenheim, D. S. Scheirer, M. J. Rymer, J. M. Stock, J. A. Hole, R. D. Catchings, *et al.* (2017). Subsurface geometry of the San Andreas fault in southern California: Results from the Salton Seismic Imaging Project (SSIP) and strong ground motion expectations, *Bull. Seismol. Soc. Am.* **107,** no. 4, 1642–1662.

Fuis, G. S., W. D. Mooney, J. H. Healy, G. A. McMechan, and W. J. Lutter (1982). Crustal structure of the Imperial Valley region, *U.S. Geol. Surv. Open-File Rept. 81-270*, Prof. Pap. 1254, 25–49.

Fuis, G. S., W. D. Mooney, J. H. Healy, G. A. McMechan, and W. J. Lutter (1984). A seismic refraction survey of the Imperial Valley region, California, *J. Geophys. Res.* **89,** 1165–1189.

Garg, S. K., J. W. Pritchett, and J. Combs (2010). Exploring for hidden geothermal systems, *Proc. of the World Geothermal Congress 2010*, Bali, Indonesia, 25–29 April 2010, 7 pp.

Gök, R., A. Kaviani, E. M. Matzel, M. E. Pasyanos, K. Mayeda, G. Yetirmishli, I. El Hussain, A. Al-Amri, F. Al-Jeri, T. Godoladze, *et al.* (2016). Moment magnitudes of local/regional events from 1D coda calibrations in the broader Middle East region, *Bull. Seismol. Soc. Am.* **106,** no. 5, 1926–1938.

Han, L., J. A. Hole, J. M. Stock, G. S. Fuis, A. Kell, N. W. Driscoll, G. M. Kent, A. J. Harding, M. J. Rymer, A. González-Fernández, *et al.* (2016). Continental rupture and the creation of new crust in the Salton trough rift, southern California and northern Mexico: Results from the Salton Seismic Imaging Project, *J. Geophys. Res.* **121,** no. 10, 7469–7489.

Hartog, A. (2000). Distributed fiber-optic sensors: Principles and applications, in *Optical Fiber Sensor Technology*, K. T. V. Grattan and B. T. MeggittSpringer, Boston, Massachusetts, doi: 10.1007/978-1-4757-6079-8_4.

Hauksson, E., J. Stock, R. Bilham, M. Boese, X. Chen, E. J. Fielding, J. Galetzka, K. W. Hudnut, K. Hutton, L. M. Jones, *et al.* (2013). Report on the August 2012 Brawley earthquake swarm in Imperial Valley, southern California, *Seismol. Res. Lett.* **84,** no. 2, 177–189.

Hauksson, E., W. Yang, and P. M. Shearer (2012). Waveform relocated earthquake catalog for southern California (1981 to June 2011), *Bull. Seismol. Soc. Am.* **102,** no. 5, 2239–2244, doi: 10.1785/0120120010.

Im, K., and J.-P. Avouac (2021). On the role of thermal stress and fluid pressure in triggering seismic and aseismic faulting at the Brawley geothermal field, California, *Geothermics* **97,** 102238, doi: 10.1016/j.geothermics.2021.102238.

Jousset, P., T. Reinsch, T. Ryberg, H. Blanck, A. Clarke, R. Aghayev, G. P. Hersir, J. Henninges, M. Weber, and C. M. Krawczyk (2018). Dynamic strain determination using fibre-optic cables allows imaging of seismological and structural features, *Nat. Commun.* **9,** no. 1, 1–11.

Kaspereit, D., M. Mann, S. Sanyal, B. Rickard, W. Osborn, and J. Hulen (2016). Updated conceptual model and reserve estimate for the Salton Sea geothermal field, Imperial Valley, California, *Geotherm. Res. Council Trans.* **40,** 57–66.

Lachenbruch, A. H., J. H. Sass, and S. P. Galanis (1985). Heat flow in southernmost California and the origin of the Salton Trough, *J. Geophys. Res.* **90,** 6709–6736.

Li, Z., and Z. Zhan (2018). Pushing the limit of earthquake detection with distributed acoustic sensing and template matching: A case study at the Brady geothermal field, *Geophys. J. Int.* **215,** no. 3, 1583–1593.

Li, Z., Z. Shen, Y. Yang, E. Williams, X. Wang, and Z. Zhan (2021). Rapid response to the 2019 Ridgecrest earthquake with distributed acoustic sensing, *AGU Adv.* **2,** no. 2, e2021AV000395, doi: 10.1029/2021AV000395.

Lindsey, N. J., and E. R. Martin (2021). Fiber-optic seismology, *Annu. Rev. Earth Planet. Sci.* **49,** 309–336.

Lindsey, N. J., T. C. Dawe, and J. B. Ajo-Franklin (2019). Illuminating seafloor faults and ocean dynamics with dark fiber distributed acoustic sensing, *Science* **366,** no. 6469, 1103–1107.

Lindsey, N. J., E. R. Martin, D. S. Dreger, B. Freifeld, S. Cole, S. R. James, B. L. Biondi, and J. B. Ajo-Franklin (2017). Fiber-optic network observations of earthquake wavefields, *Geophys. Res. Lett.* **44,** no. 23, 11,792–11,799.

Lindsey, N. J., H. Rademacher, and J. B. Ajo-Franklin (2020). On the broadband instrument response of fiber-optic DAS arrays, *J. Geophys. Res.* **125,** no. 2, e2019JB018145, doi: 10.1029/2019JB018145.

Lindsey, N. J., S. Yuan, A. Lellouch, L. Gualtieri, T. Lecocq, and B. Biondi (2020). City-scale dark fiber DAS measurements of infrastructure use during the COVID19 pandemic, *Geophys. Res. Lett.* **47,** no. 16, e2020GL089931, doi: 10.1029/2020GL089931.

Mateeva, A., J. Mestayer, B. Cox, D. Kiyashchenko, P. Wills, J. Lopez, S. Grandi, K. Hornman, P. Lumens, A. Franzen, and D. Hill (2012). Advances in distributed acoustic sensing (DAS) for VSP, *In SEG Technical Program Expanded Abstracts 2012*, Society of Exploration Geophysicists 1–5.

Matlick, S., and T. Jayne (2008). Resurrection of a previously developed geothermal field, *Geotherm. Res. Council Trans.* **32,** 159–161.

McGuire, J. J., R. B. Lohman, R. D. Catchings, M. J. Rymer, and M. R. Goldman (2015). Relationships among seismic velocity, metamorphism, and seismic and aseismic fault slip in the Salton sea geothermal field region, *J. Geophys. Res.* **120,** no. 4, 2600–2615.

Miller, D. E., T. M. Daley, D. White, B. M. Freifeld, M. Robertson, J. Cocker, and M. Craven (2016). Simultaneous acquisition of distributed acoustic sensing VSP with multi-mode and single-mode fibre-optic cables and 3C-geophones at the Aquistore CO_2 storage site, *CSEG Recorder* **41,** no. 6, 28–33.

Nayak, A., J. Ajo-Franklin, and Imperial Valley Dark Fiber Team(2021). Distributed acoustic sensing using dark fiber for array detection of regional earthquakes, *Seismol. Res. Lett.* **92,** 2441–2452.

Ormat Nevada Inc. (2017). Wister, CA downhole and seismic data [data set], doi: 10.15121/1441453.

Paitz, P., P. Edme, D. Gräff, F. Walter, J. Doetsch, A. Chalari, C. Schmelzbach, and A. Fichtner (2021). Empirical investigations of the instrument response for distributed acoustic sensing (DAS) across 17 octaves, *Bull. Seismol. Soc. Am.* **111,** no. 1, 1–10.

Persaud, P., Y. Ma, J. M. Stock, J. A. Hole, G. S. Fuis, and L. Han (2016). Fault zone characteristics and basin complexity in the southern Salton trough, California, *Geology* **44,** no. 9, 747–750.

Pinzon-Rincon, L., F. Lavoué, A. Mordret, P. Boué, F. Brenguier, P. Dales, Y. Ben-Zion, F. Vernon, C. J. Bean, and D. Hollis (2021). Humming trains in seismology: An opportune source for probing the shallow crust, *Seismol. Res. Lett.* **92,** no. 2A, 623–635.

Quiros, D. A., L. D. Brown, and D. Kim (2016). Seismic interferometry of railroad induced ground motions: Body and surface wave imaging, *Geophys. J. Int* **205,** no. 1, 301–313.

Ram Power Inc. (2013). New river geothermal exploration (Ram Power Inc.) [data set], doi: 10.15121/1148796.

Robertson-Tait, A., W. Harvey, S. Hamm, and L. Boyd (2021). The United States of America country update 2020—Power generation, *Proc. of the World Geothermal Congress 2020+1*, Reykjavik, Iceland, April–October 2021, 15 pp.

Rodríguez Tribaldos, V., and J. B. Ajo-Franklin (2021). Aquifer monitoring using ambient seismic noise recorded with distributed acoustic sensing (DAS) deployed on dark fiber, *J. Geophys. Res.* **126,** no. 4, e2020JB021004, doi: 10.1029/2020JB021004.

Ryan, G. A., and E. Shalev (2014). Seismic velocity/temperature correlations and a possible new geothermometer: Insights from exploration of a high-temperature geothermal system on Montserrat, West Indies, *Energies* **7,** no. 10, 6689–6720.

Siler, D. L., and B. M. Kennedy (2016). Regional crustal-scale structures as conduits for deep geothermal upflow, *Geothermics* **59,** 27–37.

Wang, H. F., X. Zeng, D. E. Miller, D. Fratta, K. L. Feigl, C. H. Thurber, and R. J. Mellors (2018). Ground motion response to an ML 4.3 earthquake using co-located distributed acoustic sensing and seismometer arrays, *Geophys. J. Int.* **213,** no. 3, 2020–2036.

Wei, S., J. P. Avouac, K. W. Hudnut, A. Donnellan, J. W. Parker, R. W. Graves, D. Helmberger, E. Fielding, Z. Liu, F. Cappa, *et al.* (2015). The 2012 Brawley swarm triggered by injection-induced aseismic slip, *Earth Planet. Sci. Lett.* **422,** 115–125.

Wessel, P., W. H. F. Smith, R. Scharroo, J. Luis, and F. Wobbe (2013). Generic Mapping Tools: Improved version released, *Eos* **94,** no. 45, 409–410.

Williams, C. F., M. J. Reed, J. DeAngelo, and S. P. Galanis Jr. (2009). Quantifying the undiscovered geothermal resources of the United States, *Geotherm. Res. Council Trans.* **33,** 995–1002.

Williams, E. F., M. R. Fernández-Ruiz, R. Magalhaes, R. Vanthillo, Z. Zhan, M. González-Herráez, and H. F. Martins (2021). Scholte wave inversion and passive source imaging with ocean-bottom DAS, *The Leading Edge* **40,** no. 8, 576–583.

Yu, C., Z. Zhan, N. J. Lindsey, J. B. Ajo-Franklin, and M. Robertson (2019). The potential of DAS in teleseismic studies: Insights from the Goldstone experiment, *Geophys. Res. Lett.* **46,** no. 3, 1320–1328.

Yuan, S., J. Liu, H. Young Noh, and B. Biondi (2021). Urban system monitoring using combined vehicle onboard sensing and roadside distributed acoustic sensing, in *First International Meeting for Applied Geoscience and Energy Expanded Abstracts*, Society of Exploration Geophysicists, 3235–3239.

Zehner, R. E., K. N. Tullar, and E. Rutledge (2012). Effectiveness of 2-meter and geoprobe shallow temperature surveys in early stage geothermal exploration, *Geotherm. Res. Council Trans.* **36,** 835–841.

Zhan, Z. (2020). Distributed acoustic sensing turns fiber-optic cables into sensitive seismic antennas, *Seismol. Res. Lett.* **91,** no. 1, 1–15.

Zhu, T., J. Shen, and E. R. Martin (2021). Sensing earth and environment dynamics by telecommunication fiber-optic sensors: An urban experiment in Pennsylvania, USA, *Solid Earth* **12,** no. 1, 219–235.

Manuscript received 2 March 2022
Published online 10 June 2022